Available online at www.sciencedirect.com

ScienceDirect

Procedia Engineering 144 (2016) 883 – 890

Procedia Engineering

www.elsevier.com/locate/procedia

12th International Conference on Vibration Problems, ICOVP 2015

Dynamical stability analysis of a fluid structure interaction system using a high fidelity Navier-Stokes solver

Chandan Bose[a], Sandeep Badrinath[b], Sayan Gupta[a], Sunetra Sarkar[b,*]

[a]*Department of Applied Machanics, Indian Institute of Technology Madras, Chennai 600 036, India*
[b]*Department of Aerospace Engineering, Indian Institute of Technology Madras, Chennai 600 036, India*

Abstract

The present paper investigates the flow induced dynamics of a non-linear fluid-structure interaction (FSI) system comprising of a symmetrical NACA 0012 airfoil supported by non-linear springs. Two methods are used in calculating the aerodynamic loads: a linear analytical approach and a full Navier-Stokes (N-S) solution. The analytical approach is based on the assumption of potential flow theory and a rigid wake. Wind velocity as a bifurcation parameter shows that the structural response undergoes a supercritical Hopf bifurcation. However, the analytical loads predict unrealistic bifurcation onset at low values of solid to fluid added mass ratio (μ) relevant to the application of flapping wing micro air vehicles (MAVs), showing the extremely large amplitude of oscillations. These observations render the use of an inviscid approach meaningless at such parametric regimes. Hence, we propose to use a N-S solver to emphasize the limit of applicability of the linear aerodynamic theory. Moreover, the inclusion of the viscous effects can potentially result in interesting dynamical behavior that has not been captured by the analytical approach. A bifurcation and stability analysis has been carried out for different parametric variations of μ in the fluid structure interaction system.

Peer-review under responsibility of the organizing committee of ICOVP 2015

Keywords: Fluid-Structure Interaction, Bifurcation analysis, Wagner's function, N-S equation, Limit-Cycle Oscillation, Micro Air Vehicles.

1. Introduction

In recent years, biologically inspired flapping wing micro air vehicles (MAVs) have garnered a lot of attention as a fluid structure interaction (FSI) problem because of being highly maneuverable and light weight and having immense potential of being utilized in surveillance and environmental monitoring, advancing our sensing and information gathering capabilities [1]. The interaction between unsteady aerodynamics and the structural flexibility (fluid-structure interaction) plays an important role in the efficient design of flapping wing micro air vehicles, since it can lead to failure of the control system through strong nonlinear interactions.

There can be various types of instabilities and bifurcations associated with nonlinear FSI system. Supercritical Hopf-bifurcation is a common one in which limit cycle oscillation (LCO) emerges from the damped response beyond a critical value of the bifurcation parameter. The supercritical Hopf-bifurcation is defined to occur at the lowest

* Corresponding author. Tel.: +91 44 2257 4024 ; fax: +91 44 2257 4024.
E-mail address: sunetra.sarkar@gmail.com

Peer-review under responsibility of the organizing committee of ICOVP 2015
doi:10.1016/j.proeng.2016.05.107

wind speed at which a given structure exhibits sustained LCO. Though the area of nonlinear aeroelastic instability analysis for large structures like wind turbine blades, bridges etc are quite well-investigated, similar studies for very tiny structured, lightweight MAVs are few. For these low Reynolds number flyers, the amplitude and frequency parameters are optimally utilized to augment the aerodynamic loads. Since the kinematics of flapping performed by the MAVs result in highly coupled nonlinearities, the design of high performance and robust MAVs can be directly benefitted from our understanding of the complex flow patterns in the kinematic parametric range where this kind of instability occurs.

Lee *et al.* [2] investigated linear and nonlinear aeroelastic models with common nonlinearities like cubic stiffness, free-play and hysteresis using the analytical approach with Wagner's function being used for load calculation. The advantage of such an analytical model is that it is computationally less expensive compared to a full N-S solution. However, the analytical model carries assumptions on the shape of the body, shedding of vortices form a rigid wake, inviscid, incompressible flow conditions and infinitesimal deflection of the airfoil from its mean position. Hence, it is important to know the applicability of these assumptions in a given parameter range. Chae *et al.* [3] recently showed that the linear potential theory is severely unconservative for predicting the onset of bifurcation in the case of a light foil in high-density fluid, since the fluid inertia forces are empirically approximated in the analytical theory to estimate aerodynamic load and moment. This shows the need for calculating the aerodynamic loads using a high fidelity Navier-Stokes solver at these parameter ranges. This has relevance to the design of modern day MAVs as they are extremely lightweight structures rapidly moving in a fluid, thereby generating a significant fluid inertial effect. Hence, the mass ratio for MAVs falls into the regime where the linear potential theory fails to predict the bifurcation onset correctly.

The area of computational aeroelasticity of flapping wings is not thoroughly explored yet. The coupling of aerodynamics, structural dynamics and flight dynamics is the critical component of MAV flight due to their small size and flight regime [4]. A nice review on the state of the art of computational aeroelasticity studies can be found in [5]. Full three dimensional and quasi three dimensional studies have been reported in [6,7]. In this paper, we have solved the incompressible flow field by a viscous N-S solver and coupled the aerodynamic loads with a nonlinear structural solver using fourth order Runge-Kutta scheme following a partitioned approach [8] to study the supercritical Hopf-bifurcation points of structural responses for a low range of solid to fluid added mass ratios (μ) as applicable to the natural flappers or MAVs.

The present paper is organized as follows: Section 2 provides the governing equations and boundary conditions along with the numerical solver details. The validation of the flow solver and the grid independence study is also presented in this section. The variation of the bifurcation point with mass ratio and the bifurcation diagrams along with the time histories and phase portraits corresponding to pre-bifurcation, at bifurcation and post-bifurcation cases have been discussed in section 3. This is followed by the description of the corresponding flow fields. The paper ends with the concluding remarks presented in section 4.

2. Numerical Implementation

There are different time marching algorithms to handle coupled FSI problems. Broadly they can be considered as i) monolithic coupling and ii) partitioned approach of coupling [9]. In the monolithic approach, the equations governing the fluid and structure are solved simultaneously at every time step, using a global discretization process that encompasses both the fluid and the solid media. This is in contrast to the partitioned approach, where two separate solvers for fluid and structure are used jointly by exchanging information from one time step to another in an alternating fashion explicitly [10]. In this present study, the partitioned approach based weak coupling method has been implemented for the numerical simulation of the FSI problem.

2.1. Flow solver

The flow is governed by the incompressible Navier-Stokes (N-S) equation. The FSI problem requires a solution over a time varying computational domain. In the present study, we use the arbitrary Lagrangian Eulerian (ALE) formulation [11] for solving the N-S equation on a moving grid. The N-S equation is cast into ALE form as,

$$\nabla.\vec{u} = 0, \tag{1}$$

$$\frac{\partial \vec{u}}{\partial t} + [(\vec{u} - \vec{u}^m).\nabla]\vec{u} = -\nabla p/\rho + \nu\nabla^2\vec{u}. \tag{2}$$

Here, $\vec{u}$ is the velocity of the flow, $\vec{u}^m$ is the grid point velocity, p is the pressure, ν is the kinematic viscosity and ρ is the fluid density. An additional constraint arising from the ALE approach is that the mesh motion satisfy the geometric conservation law [12] given by Eq. (3). The geometric conservation law ensures that the change in cell volume after each time step is equal to the cell volume ($\forall$) swept by the cell boundary and can be expressed as,

$$\frac{\partial \forall}{\partial t} + \nabla.u^m = 0. \tag{3}$$

A mesh motion algorithm is required for the ALE method to compute the positions of the internal grid points based on the boundary movement at each time step. Different mesh motion strategies have been used earlier, which can be applied on both structured and unstructured grids. However, an important aspect of any mesh motion algorithm is to preserve the mesh quality with good computational efficiency. In the present study, Radial Basis Function (RBF) interpolation is used to find the displacements of the internal grid points for a given boundary displacement [13]. RBF interpolation provides superior mesh quality near the moving body even for large displacements and rotations compared to other mesh motion solver.

The simulations are performed in OpenFOAM [14], an open source finite-volume based CFD solver. The spatial and temporal discretizations are carried out using second order accurate schemes. A variable time stepping is used corresponding to a maximal Courant number for an efficient solution. The pressure-velocity coupling is achieved through Pressure implicit with splitting of operator (PISO) algorithm. The algorithms used here for solving the pressure, velocity and mesh motion have been discussed in detail by Bos [15].

2.2. Structural solver

The structural part is comprised of an airfoil (semi chord length of 'b') with pitch-plunge degrees of freedom as shown in Fig. 1. The airfoil is restrained by non-linear springs and the elastic axis passes through the quarter chord position. The direction of positive lift and moment is indicated in the figure.

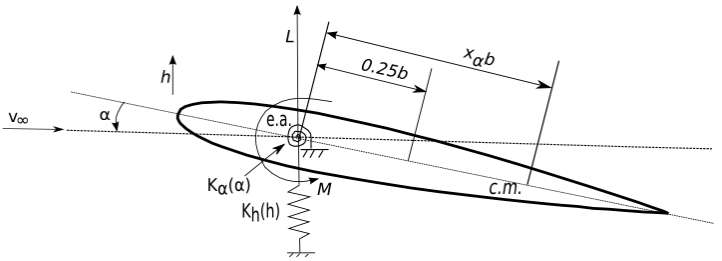

Fig. 1. Schematic of a symmetric airfoil in pitch and plunge degrees of freedom

The equations of motion are given by [2],

$$m\ddot{h} + S\ddot{\alpha} + C_h\dot{h} + K_h(h) = L(t) \;\; where \;\; k_h(h) = K_{h1}h + K_{h2}h^3, \tag{4}$$

$$S\ddot{h} + I\ddot{\alpha} + C_\alpha\dot{h} + k_\alpha(\alpha) = M(t) \;\; where \;\; k_\alpha(\alpha) = K_{\alpha1}\alpha + K_{\alpha2}\alpha^3. \tag{5}$$

In the above equation, m is the mass of the airfoil, S is the first moment of inertia, I is the second moment of inertia; K_{h1}, K_{h2}, $K_{\alpha1}$ and $K_{\alpha2}$ are the spring stiffness coefficients; C_h and C_α are the damping coefficients; $L(t)$ is the unsteady lift and $M(t)$ is the moment about the quarter chord.
The expressions for inertia and stiffness parameters are given by Lee *et al.*[2],

$$S = mx_\alpha b;\; I = mr_\alpha{}^2b^2;\; K_{h1}{}^2 = m\omega_h^2;\; K_{\alpha1}{}^2 = I\omega_\alpha^2;\; K_{h2} = \beta_h K_{h1};\; K_{\alpha2} = \beta_\alpha K_{\alpha1}. \tag{6}$$

Here, b is the semi-chord, $r_\alpha b$ is the radius of gyration, $x_\alpha b$ is the distance between the center of mass and elastic center; ω_h and ω_α are the uncoupled natural frequencies of pitch and plunge respectively; β_h and β_α determine the extent of non-linearity in the spring stiffness.

Following Lee et al. [2], we define the following non-dimensional variables,

$$U^* = \frac{v_\infty}{b\omega_\alpha};\ \tau = \frac{v_\infty t}{b};\ \bar{\omega} = \frac{\omega_h}{\omega_\alpha};\ \mu = \frac{m}{\pi\rho b^2}. \tag{7}$$

Here, U^* and τ correspond to the non-dimensional velocity and time, $\bar{\omega}$ and μ are referred as the frequency ratio and mass ratio respectively. The structural response (Eq. 4-5) has been solved using a fourth-order Runge-Kutta method. The time step for integration is equal to that of the flow solver. The flow solver has a more stringent requirement on the time step, thus assuring convergence for the structural equation.

2.3. Coupling between flow solver and structural solver

In the present partitioned based FSI scheme, each physical region (the fluid and the solid) is treated with its own numerical solver. The interaction between these regions is manifested through the boundary conditions of their corresponding solver. This strategy has proved to be reliable in classical aeroelastic problems [8]. Hence, it is used in the present investigation. The coupling scheme is explained in the flowchart below:

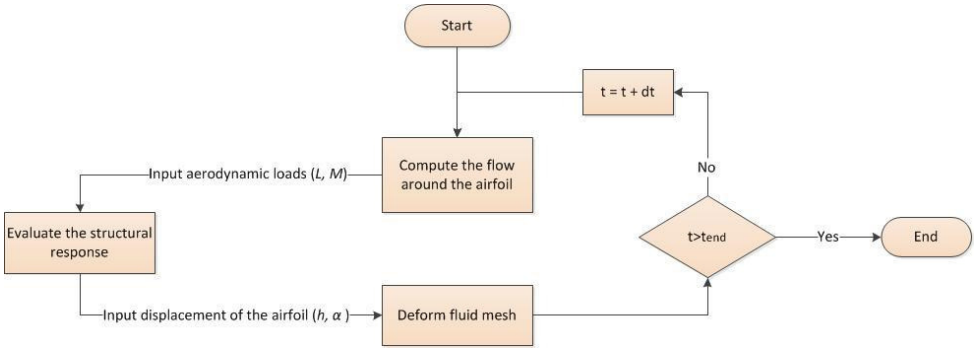

2.4. Computational domain and grid independence tests

A rectangular computational domain shown in Fig. 2 (a) was used for the analysis. The figure also shows the boundaries and dimensions of the computational domain. Standard boundary conditions are applied: a zero pressure gradient condition and a constant free-stream at the inlet, a zero velocity gradient and atmospheric pressure condition at the outlet and no slip and zero normal pressure gradient condition on the walls and the airfoil surface. The computational domain is discretized using a combination of structured and unstructured grids. A structured mesh was used around the airfoil in the near-field and an unstructured mesh was used for the far-field as shown in Fig. 2 (b).

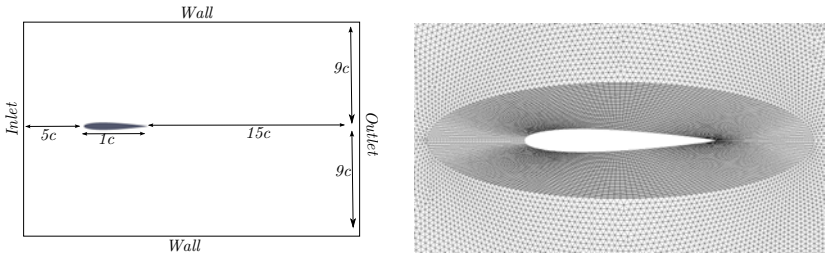

Fig. 2. (a) Computational domain for the analysis (not to scale), (b) A close-up view of the computational grid around the airfoil

The mesh used for the analysis was chosen after a grid independence test. The test was performed by comparing the aerodynamic load (C_l) using grids of different resolutions. The grid resolution was increased by increasing the

number of grid points on the airfoil. We present the grid convergence at a high non-dimensional plunge velocity (kh) for a pure plunging case, where k is the reduced frequency and h is the nondimensional plunge amplitude. The results of the grid convergence are shown in Fig. 3 (a) for three different grid resolutions. The figure confirms the convergence of the mesh with 200 grid points on the airfoil as the lift coefficient closely matches with the mesh of higher resolution (with 250 points on the airfoil). Hence, the mesh with 200 grid points on the airfoil (containing 82,372 grid points in total) is chosen for further analysis.

2.5. Flow solver validation

The solver was validated by comparing the aerodynamic loads obtained from the present computation with earlier experiments performed by Cleaver *et al.* [16]. They have performed force measurements for a NACA0012 airfoil with sinusoidal plunge kinematics at various amplitudes and frequencies in a water tunnel at $Re = 10,000$. Fig. 3 (b) shows the comparison of the time-averaged drag coefficients at different k for $h = 0.1$ & 0.15. The time-averaged drag coefficient for the present computation was calculated by performing simulations for 10 cycles and then calculating the average over the last 4 cycles. This methodology has been adopted since the aerodynamic loads become aperiodic at high values of kh [17]. The comparison of the drag coefficient between the experimental results and the present computation shows a good agreement and this confirms the validity of the flow solver.

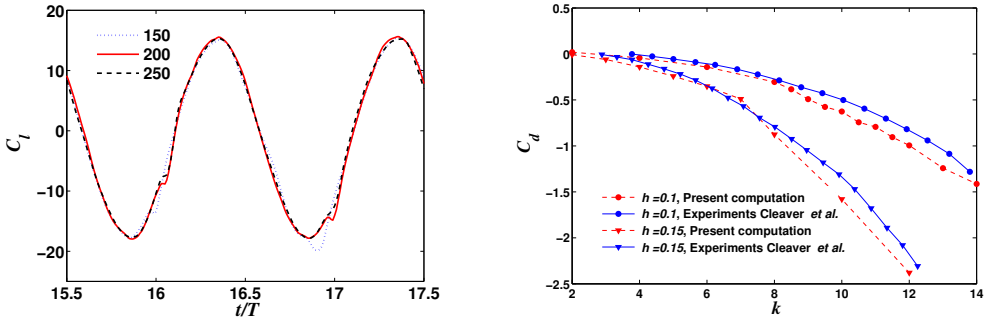

Fig. 3. (a) The comparison of the lift coefficient for different number of grid points on the airfoil, (b)Comparison of drag coefficient with experimental measurements of Cleaver et al. [15] for a plunging airfoil with kinematic parameters k=2, h = 0.1, 0.15 and Re=10,000

3. Results and discussions

3.1. Variation of bifurcation onset with mass ratio

The structural response undergoes supercritical Hopf bifurcation with the non-dimensional wind velocity as the control parameter. The bifurcation points (U_f^*), obtained using the analytical and N-S based flow solvers, are plotted as a function of solid to fluid added mass ratio (μ) in Fig. 4. The variation of supercritical Hopf bifurcation point, obtained using analytical flow solver, shows steady decrease till around $\mu = 4$ and beyond which it shows a sharp increase which is unrealistic and against earlier experimental observations [3]. The bifurcation points (U_f^*) obtained using N-S based solver closely match the analytical values up to around $\mu = 10$. However, below some critical μ value, analytical solver predictions are unrealistic as the trend gets reversed. Hence, approximate modeling of the fluid inertia forces in the analytical solver is clearly not suitable when the structural and fluid added mass effects are comparable. On the other hand, the N-S based solver is able to predict realistic onset values at the entire regime.

3.2. Bifurcation diagrams

Fig. 5 plots the bifurcation diagrams of pitch and plunge responses respectively for $\mu = 2$ and $\mu = 5$ for both analytical and N-S based solver. For $\mu = 5$, the bifurcation point is predicted by the viscous solver as $U_f^* = 1.2$

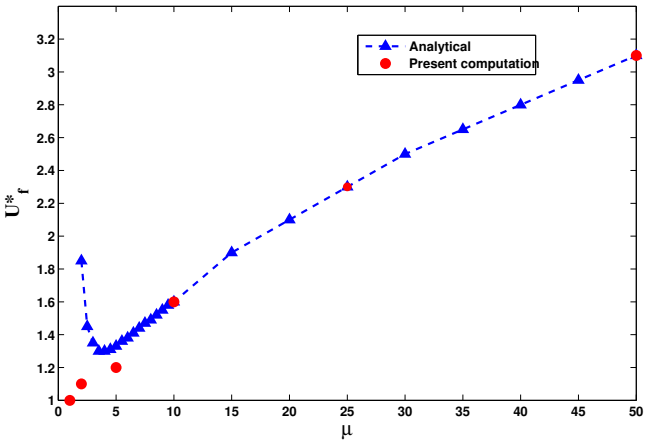

Fig. 4. The comparison of bifurcation point varying with μ between analytical and N-S solver results

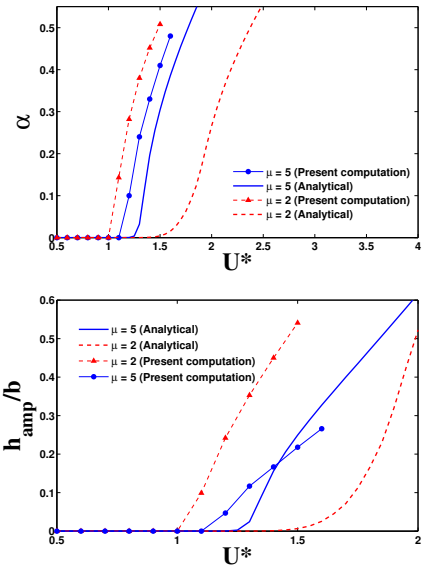

Fig. 5. Comparison of bifurcation diagram of (a) pitch and (b) plunge corresponding to $\mu = 2$ and $\mu = 5$

whereas the analytical solver predicts it as $U_f^* = 1.33$ and for $\mu = 2$, it is predicted as $U_f^* = 1.1$ by the viscous solver and $U_f^* = 1.85$ by the analytical solver. The comparative study vividly depicts that the analytical solver is unconservative and with decreasing μ value, it gives more unrealistic values of the onset of LCO. Hence as μ is decreased, the bifurcation point predicted by analytical solver will diverge from that of predicted by the viscous solver and below $\mu = 2$, the analytical solver fails to determine the bifurcation point due to numerical limitation whereas the N-S based solver is valid in the entire regime.

3.3. Time series, phase portrait and FFT of the structural response at $\mu = 2$

Time histories of pitch and plunge responses obtained from both the viscous and analytical solver for $\mu = 2$ are presented in Fig. 6 & Fig. 7 for non-dimensional wind speed U^*= 1, 1.1 and 1.2 to understand the nature of the responses for pre-bifurcation, bifurcation and post-bifurcation regimes respectively. It can be observed that the pitch and plunge responses obtained from viscous solver show damped oscillations at $U^* = 1$; show sustained oscillation at $U^* = 1.1$ and 1.2, though the latter case shows higher amplitude. Hence it can be concluded that a super-critical Hopf-bifurcation has taken place at $U^* = 1.1$ below which zero is a stable fixed point and beyond which the stationary limit cycle is a stable one dimensional attractor of the dynamical system. This can be observed from the corresponding phase portrait of pitch response at pre-bifurcation onset, at bifurcation onset and post-bifurcation onset respectively, shown in Fig. 8 (a)-(c). All the time histories obtained from the analytical solver at $U^* = 1$, 1.1 and 1.2 are damped response, since the onset of the bifurcation happens at $U^* = 1.85$ as per the analytical solver. The existence of a single frequency self sustained LCO is verified by a single peak in the frequency spectra of the structural response as shown in the Fig. 8 (d). The frequency of the LCO is obtained as 0.7629 Hz (4.79 rad/sec) which is in between ω_h (4 rad/sec) and ω_α (5 rad/sec).

3.4. Flow fields

The flow patterns corresponding to pre-bifurcation regime, at bifurcation point and post-bifurcation regime are presented in terms of vorticity contours in Fig. 9 at various time instances for $\mu = 2$. It can br clearly observed in the vorticity pattern that prior to the onset of limit cycle oscillation, the damped response subsequently leads to a Von Karman vortex street beyond transience which corresponds to the natural shedding past the fixed airfoil. However,

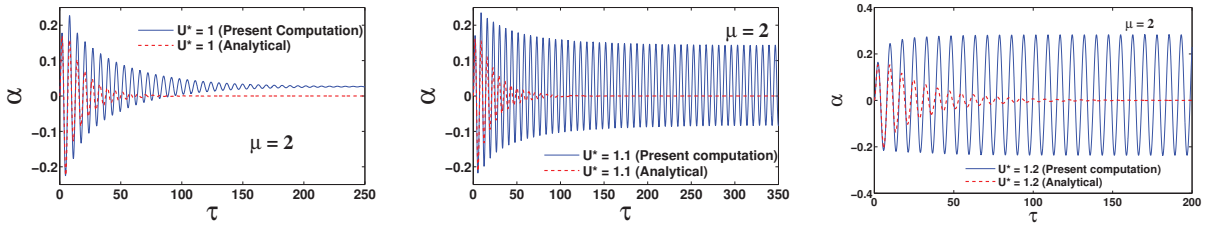

Fig. 6. Time series of pitch for (a) U^* = 1, (b) U^* =1.1, (c) U^* =1.2

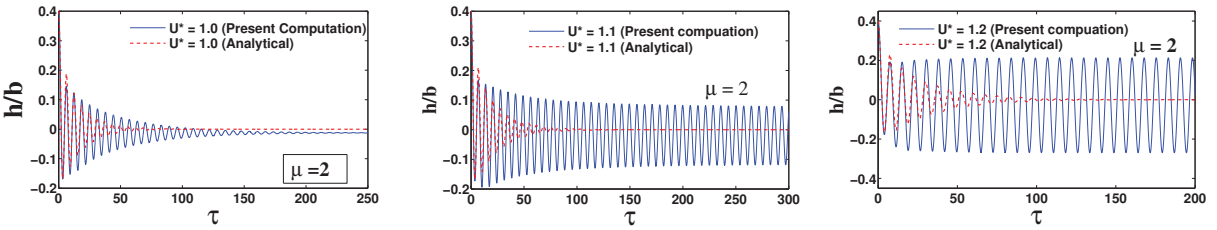

Fig. 7. Time series of plunge for (a) U^* = 1, (b) U^* =1.1, (c) U^* =1.2

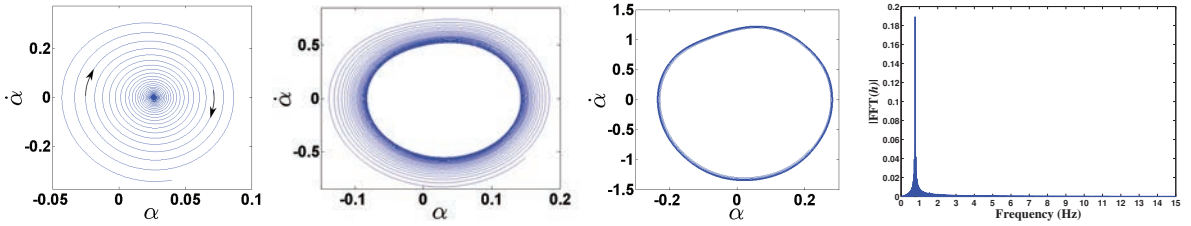

Fig. 8. Phase portrait of pitch (present computation) for (a) U^* = 1, (b) U^* =1.1, (c) U^* =1.2 and (d) FFT of the pitch response at U* = 1.1

trailing-edge vorticity contours past the airfoil oscillating in stable limit cycle beyond the bifurcation point, sustains the same pattern in downstream. Clearly there are two time scales involved in the trailing edge flow pattern. The large time scale denotes the time period corresponding to LCO of the structural response and the smaller time scale relates to the time period of the natural shedding past an airfoil. In the post-bifurcation regime, the amplitude of the larger timescale of trailing edge wake pattern increases which relates to the higher amplitude LCO as shown in the figure.

4. Conclusion

In the present work, a nonlinear FSI model has been developed using a high-fidelity N-S solver. The dynamical behavior in terms of the Hopf-bifurcation point is compared with an inviscid analytical solver. It has been shown that at low values of solid to fluid added mass ratios (μ), likely to be encountered by light weight MAVs, the analytical solver fails to predict realistic solutions, highlighting the need of a full viscous model. The N-S model is able to provide realistic bifurcation points at the mentioned parameter range. It also presents interesting flow-field patterns. For the future work, the authors are working on developing a full fidelity structural solver to integrate with the N-S solver for implementing in more generic FSI applications.

References

[1] W. Shyy, H. Aono, S. K. Chimakurthi, P. Trizila, C.-K. Kang, C. E. Cesnik, H. Liu, Recent progress in flapping wing aerodynamics and aeroelasticity, Progress in Aerospace Sciences 46 (2010) 284–327.

[2] B. Lee, S. Price, Y. Wong, Nonlinear aeroelastic analysis of airfoils: bifurcation and chaos, Progress in aerospace sciences 35 (1999) 205–334.

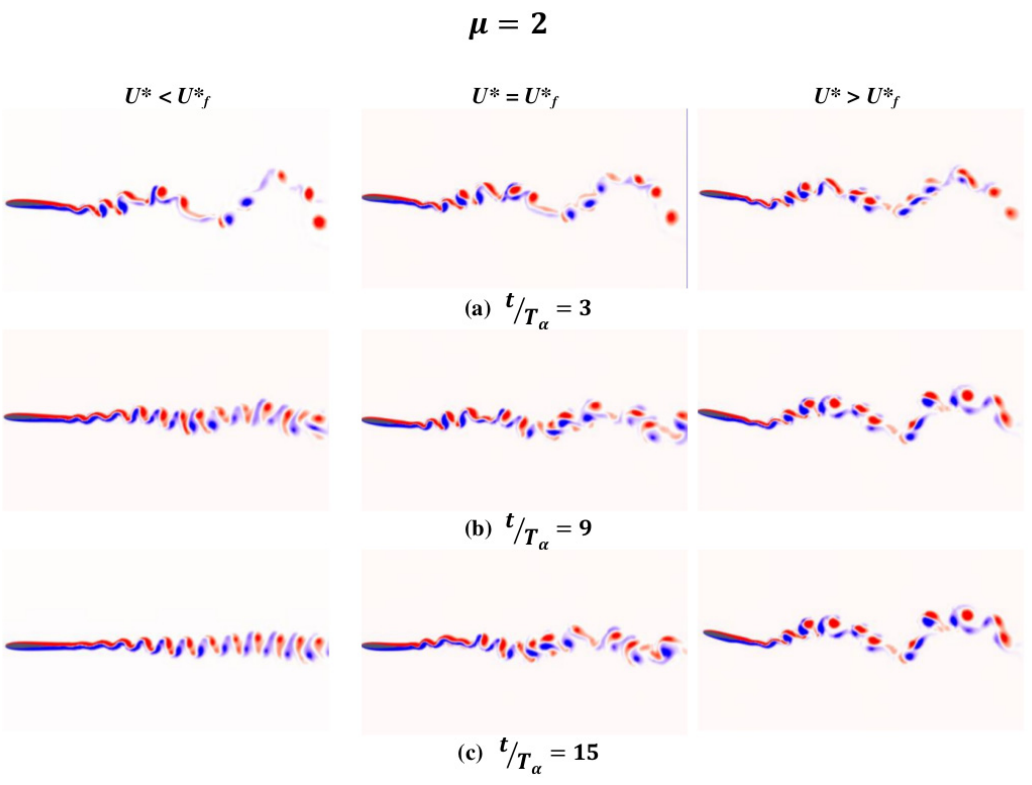

Fig. 9. Vorticity contours for U^*=1.0, 1.1, and 1.2 at different time instances at $\mu = 2$

[3] E. J. Chae, D. T. Akcabay, Y. L. Young, Dynamic response and stability of a flapping foil in a dense and viscous fluid, Physics of Fluids (1994-present) 25 (2013) 104106.
[4] S. K. Chimakurthi, B. K. Stanford, C. E. Cesnik, W. Shyy, Flapping wing cfd/csd aeroelastic formulation based on a co-rotational shell finite element, in: 50th SDM Conference, 2009, pp. 4–7.
[5] S. K. Chimakurthi, J. Tang, R. Palacios, C. E. S. Cesnik, W. Shyy, Computational aeroelasticity framework for analyzing flapping wing micro air vehicles, AIAA journal 47 (2009) 1865–1878.
[6] Y. Lian, W. Shyy, Numerical simulations of membrane wing aerodynamics for micro air vehicle applications, Journal of Aircraft 42 (2005) 865–873.
[7] J. Tang, S. Chimakurthi, R. Palacios, C. E. Cesnik, W. Shyy, Computational fluid-structure interaction of a deformable flapping wing for micro air vehicle applications, in: 46th AIAA Aerospace Sciences Meeting and Exhibit, 2008, pp. 7–10.
[8] C. Farhat, M. Lesoinne, Two efficient staggered algorithms for the serial and parallel solution of three-dimensional nonlinear transient aeroelastic problems, Computer methods in applied mechanics and engineering 182 (2000) 499–515.
[9] D. Trimarchi, Analysis of downwind sail structures using non-linear shell finite elements: wrinkle development and fluid interaction effects, Ph.D. thesis, University of Southampton, 2012.
[10] C. Michler, S. Hulshoff, E. Van Brummelen, R. De Borst, A monolithic approach to fluid–structure interaction, Computers & fluids 33 (2004) 839–848.
[11] J. Ferziger, M. Peric, Computational Methods for Fluid Dynamics,3rd edition, Springer-Verlag, Berlin, 2002.
[12] P. D. Thomas, C. K. Lombard, Geometric conservation law and its application to flow computations on moving grids, AIAA Journal 17(10) (1979) 1030 – 1037.
[13] F. M. Bos, B. W. Van Oudheusden, H. Bijl, Radial basis function based mesh deformation applied to simulation of flow around flapping wings, Computers and Fluids 79 (2013) 167–177.
[14] OpenFOAM, The Open Source CFD Toolbox User Guide., 2013. URL: `http://www.openfoam.org/`.
[15] F. M. Bos, Numerical simulations of flapping foil and wing aerodynamics, Ph.D. thesis, TU Delft, 2010.
[16] D. J. Cleaver, Z. Wang, I. Gursul, High-order accurate simulations of unsteady flow past plunging and pitching airfoils, Journal of Fluid Mechanics 708 (2012) 349–376.
[17] M. A. Ashraf, J. Young, J. S Lai, Oscillation frequency and amplitude effects on plunging airfoil propulsion and flow periodicity, AIAA Journal 50 (2012) 2308–2324.